Journal of Nanobiotechnology

RESEARCH

Open Access

Ellagic acid-enhanced biocompatibility and bioactivity in multilayer core-shell gold nanoparticles for ameliorating myocardial infarction injury

Xina Yu[1], Jie Wang[2], Tiantian Wang[1], Shanshan Song[1], Hongna Su[1], Hui Huang[4] and Pei Luo[1,3*]

Abstract

Background Myocardial infarction (MI) is the main contributor to most cardiovascular diseases (CVDs), and the available post-treatment clinical therapeutic options are limited. The development of nanoscale drug delivery systems carrying natural small molecules provides biotherapies that could potentially offer new treatments for reactive oxygen species (ROS)-induced damage in MI. Considering the stability and reduced toxicity of gold-phenolic core-shell nanoparticles, this study aims to develop ellagic acid-functionalized gold nanoparticles (EA-AuNPs) to overcome these limitations.

Results We have successfully synthesized EA-AuNPs with enhanced biocompatibility and bioactivity. These core-shell gold nanoparticles exhibit excellent ROS-scavenging activity and high dispersion. The results from a label-free imaging method on optically transparent zebrafish larvae models and micro-CT imaging in mice indicated that EA-AuNPs enable a favorable excretion-based metabolism without overburdening other organs. EA-AuNPs were subsequently applied in cellular oxidative stress models and MI mouse models. We found that they effectively inhibit the expression of apoptosis-related proteins and the elevation of cardiac enzyme activities, thereby ameliorating oxidative stress injuries in MI mice. Further investigations of oxylipin profiles indicated that EA-AuNPs might alleviate myocardial injury by inhibiting ROS-induced oxylipin level alterations, restoring the perturbed anti-inflammatory oxylipins.

Conclusions These findings collectively emphasized the protective role of EA-AuNPs in myocardial injury, which contributes to the development of innovative gold-phenolic nanoparticles and further advances their potential medical applications.

Keywords Polyphenols, Gold nanoparticles, Biocompatibility, Oxidative stress, Oxylipins, Myocardial infarction

*Correspondence:
Pei Luo
pluo@must.edu.mo

Full list of author information is available at the end of the article

Graphical Abstract

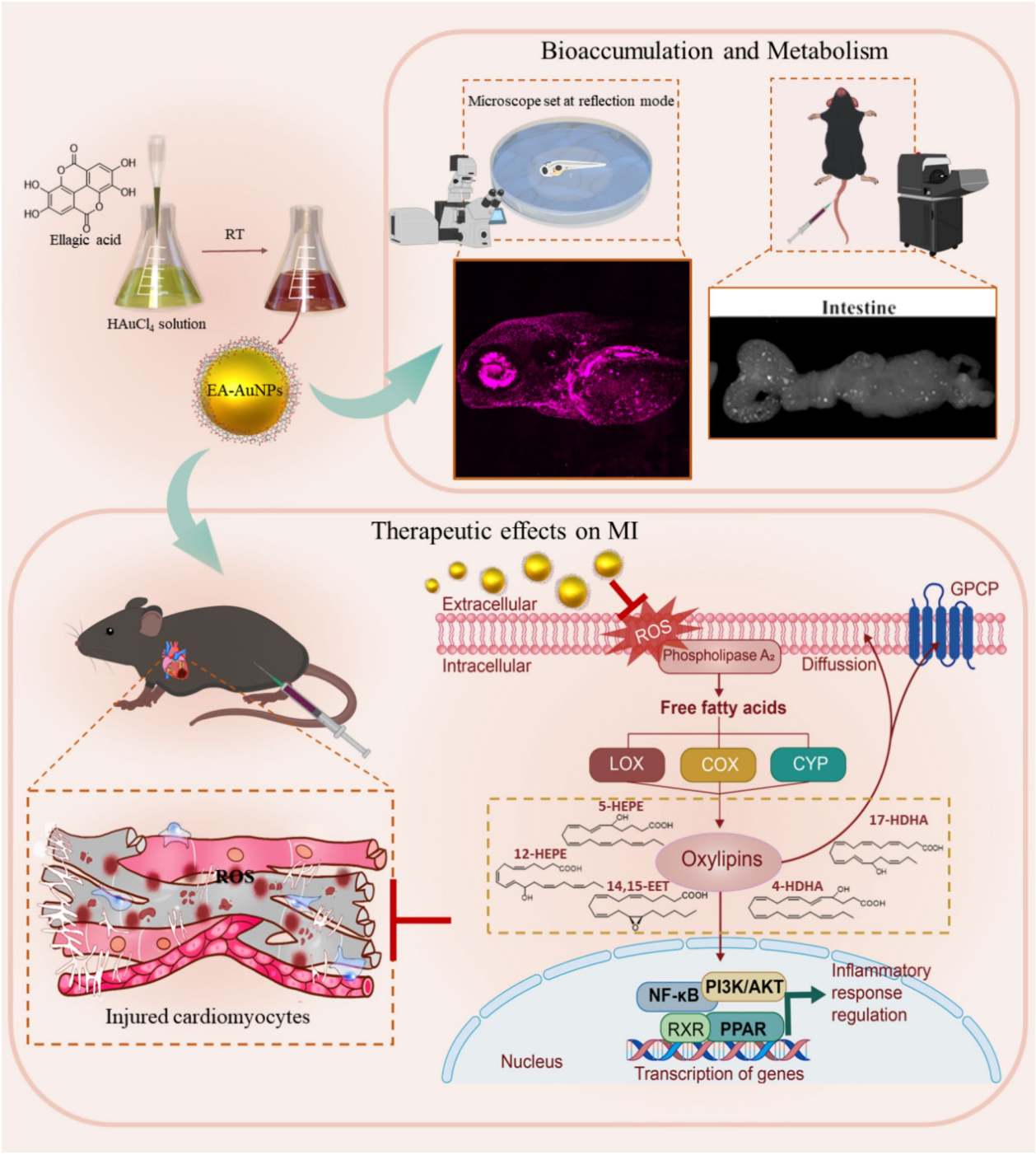

Introduction

Myocardial infarction (MI), the main contributor to death and disability worldwide [1], leads to the thinning of the ventricular wall [2], the formation of a fibrous scar in the left ventricle, and a reduction in cardiac function, ultimately resulting in heart failure [3]. At present, some clinical treatments, including reperfusion therapy, coronary stent implantation, and drug therapy, are commonly used to mitigate cardiac tissue damage caused by MI. Reperfusion therapy aims to restore blood flow to the obstructed areas and reduce myocardial necrosis. However, the reintroduction of oxygen and the overload of

intracellular calcium ions (Ca^{2+}) during the reperfusion process may further exacerbate cardiomyocyte necrosis and mitochondrial dysfunction [4], potentially enlarging the infarction area [5]. Although invasive surgeries are the most direct and effective treatment for MI, their applicability is restricted due to specific indications for some patients [6]. Additionally, pharmacological agents, including β-receptor blockers, nitrate drugs, angiotensin-converting enzyme inhibitors (ACEIs), and statins, may be insufficient for some patients due to their short half-life and the risk of severe side effects [7–9]. The post-MI microenvironment also significantly restricts the therapeutic efficacy of these drugs. After MI, apoptotic cardiomyocytes generate a substantial quantity of reactive oxygen species (ROS). These ROS serve dual roles as signaling molecules and inflammatory mediators, significantly influencing the progression of subsequent pathological processes and other complications [10]. Excessive ROS can trigger lipid peroxidation within cell membranes, disrupt the homeostasis of cardiomyocytes, provoke the secretion of proinflammatory cytokines, and recruit macrophages to the injured myocardium [11]. The inflammatory reaction in the infarcted region stimulates macrophage proliferation and the development of a fibrotic microenvironment [12], which in turn amplifies inflammation and cardiac remodeling, potentially culminating in heart failure. Therefore, there is an urgent need to develop new anti-MI drugs with fewer side effects and superior ROS scavenging capabilities.

Recently, nanoscale drug delivery systems carrying natural small molecule formulations have garnered significant attention due to their reduced side effects, improved bioavailability, and sustained release profiles [13, 14]. Notably, gold nanoparticles (AuNPs) are extensively employed in the biomedical field because of their high surface reactivity, inertness, low toxicity, and biological activity [15, 16]. Their relatively simple synthesis process, adjustable specific properties, and controlled size fabrication make AuNPs suitable platforms for various biomedical applications [17, 18]. However, chemical synthesis, the most common method for producing AuNPs, often involves toxic chemical stabilizing and reducing agents, which are undesirable for clinical and biomedical use [19]. Physical methods for AuNP production are not only hazardous and costly but also typically result in low yields and require expensive equipment and harsh reaction conditions. The development of a cost-effective method for synthesizing highly stable and biocompatible AuNPs with simple structures remains a challenge for potential large-scale production and future clinical applications.

Polyphenols, naturally occurring compounds found in fruits, vegetables, and herbs as secondary metabolites, exhibit potential pharmacological activities such as immune modulation, intrinsic antioxidant properties, anti-inflammatory effects, and anti-angiogenesis effects [20]. Gold-phenolic core-shell nanoparticle construction methods have been proposed to enhance the stability, controlled release, and higher loading capacity of these bioactive compounds, as well as to improve the biocompatibility of AuNPs [21–23]. More critically, by incorporating microscale capabilities into carrier-free self-delivery systems, the absorption of natural polyphenols into the blood circulation system can be minimized, thereby preventing undesirable side effects throughout the body [24]. However, some crucial problems in the clinical application of these gold-phenolic core-shell nanoparticles, including their bioaccumulation pattern, metabolic route, and stability, have not yet been clarified [25, 26]. Although some studies have reported the cardioprotective effects of gold-phenolic core-shell nanoparticles, none has yet investigated the pro- and anti-inflammatory oxylipins in the serum of nanoparticle-treated MI mice. Currently, the development of gold-phenolic core-shell nanoparticles for biomedical applications is still in its infancy.

Here, we describe a straightforward and rapid method for synthesizing gold-phenolic core-shell nanoparticles with a high loading capacity, utilizing a selection of phenolic compounds. Notably, the ellagic acid-functionalized gold nanoparticles (EA-AuNPs) are particularly distinguished for their exceptional dispersibility and biocompatibility. They also support a desirable excretion-based metabolism without overburdening other organs. EA-AuNPs have been shown to mitigate apoptosis and scavenge excessive ROS, thereby effectively protecting cardiomyocytes against H_2O_2-induced stimulation. Moreover, EA-AuNPs showed promising protective and therapeutic effects in an isoproterenol (ISO)-induced MI mouse model by alleviating oxidative stress injuries. Surprisingly, our research has also unveiled that EA-AuNPs can reverse the disturbance of anti-inflammatory oxylipins in ISO-treated mice, indicating that the regulation of these oxylipins may be a key mechanism through which EA-AuNPs exert their bioactive effects on MI mice. Our findings not only demonstrated the remarkable bioactivity of EA-AuNPs but also promoted the development of other biocompatible metal nanoparticles, enabling their potential applications in medical areas.

Materials and methods

Synthesis of AuNPs using polyphenols

Four milliliters of $HAuCl_4$ solution (1 mM) was added to a centrifuge tube, followed by the addition of 1 mL of phenolic compounds (0.5 mM). The mixture was stirred for 60 min at room temperature. The amount of phenolic compounds and the total volume of the system were kept constant at room temperature, while the amount of chloroauric acid was varied to maintain molar ratios of

$HAuCl_4$ to polyphenols at 1:5, 2:5, 3:5, 4:5, and 8:5. The supernatant was removed by centrifugation at 3200 rpm for 8 min to remove Au^+ as well as any unreacted material on the surface of the AuNPs. The resulting precipitate was then dispersed in distilled water and stored at 4 °C for subsequent applications.

Chemical stability test

The stability of the gold-phenolic core-shell nanoparticles was assessed by incubating them with various volumes of 1 M NaCl, 0.1 M HCl, and FBS, and by adjusting the temperature. The characteristic absorption spectra of these nanoparticles in different media and at different temperatures were recorded using a SpectraMax paradigm mutimode microplate reader (Molecular Devices, USA).

Characterization of the EA-AuNPs

The surface micromorphology, shape, and size of the EA-AuNPs were observed using transmission electron microscopy (TEM, JEM-1200EX, Japan) and atomic force microscopy (AFM, Bruker Dension Icon, Germany). The crystalline structure of the EA-AuNPs was analyzed by X-ray diffraction (XRD) with a current intensity of 40 mA and an operating voltage of 40 kV at a 2θ angle pattern. The crystalline structure of the EA-AuNPs was recorded by selected area electron diffraction (SAED) on an FEI Tecnai G2 F30 instrument operated at an acceleration voltage of 300 kV. The functional characteristics and possible interactions of the EA-AuNPs were identified using a Fourier transform infrared (FT-IR) spectrophotometer (Nicolet IS 10, USA) in the range of 400–4000 cm^{-1} at a resolution of 0.4 cm^{-1}. The elemental information of the EA-AuNPs was recorded by energy-dispersive X-ray spectroscopy (EDS) using a Phenom ProX G6 instrument operated at 15 kV.

Determination of ellagic acid assembly efficiency

The efficiency of ellagic acid assembly was determined using ultrahigh-performance liquid chromatography (UHPLC) on an Agilent 1290 UHPLC system (Agilent Technologies, Waldbronn, Germany) equipped with an ACQUITY HSS T3 column (2.1×100 mm, 1.8 μm particle size, Waters, USA). The gradient elution program consisted of mobile phase A (deionized water) and mobile phase B (acetonitrile), with the following gradient profile: 0–2 min, 16-19% v/v B; 2–6 min, 19% v/v B. The flow rate and column temperature were set at 0.15 mL/min and 30 °C, respectively. The injection volume was 2 μL, and the wavelength was set at 254 nm. The synthesized EA-AuNPs were first centrifuged at 3200 rpm for 8 min. The supernatant, containing free ellagic acid, was then collected, diluted 1:40 in methanol, and injected. The peak areas of the supernatant were brought into the external calibration curves and converted. The compound (ellagic acid only) utilized in this experiment was identified using the NMR (^1H- and ^{13}C-) spectrum (Fig. S1).

The loading efficiency of ellagic acid was calculated using the following formula:

Ellagic acid assembly efficiency (%) = (total ellagic acid used − amount of ellagic acid detected × 40)/total ellagic acid used × 100.

In vitro biocompatibility assay

For the in vitro biocompatibility assay, the THP-1 and H9c2 cell lines were used. EA-AuNPs and AuNPs, obtained through sodium citrate reduction, were tested at increasing concentrations ranging from 6.25 to 800 μg/mL. These nanoparticles were incubated with the differentiated THP-1 and H9c2 cells for 24 h. Subsequently, cell viability, intracellular ROS content, and cell apoptosis were assessed using an MTT assay, dichlorodihydrofluorescein diacetate (DCFH-DA) probe, and an Annexin V-FITC/7-AAD double-staining assay.

Zebrafish live imaging and quantification

All A/B wild-type zebrafish (*Danio rerio*) used in this experiment were maintained and bred at Hangzhou Hunter Biotechnology Co., Ltd. (Hangzhou, China) in accordance with the standards of the international AAALAC certification (certification number: 001458). Zebrafish embryos were collected and then cultured in a breeding tank at 28 °C with fresh reverse osmosis water (200 mg of instant sea salt per 1 L of water). One day post-fertilization, 0.03% 1-phenyl 2-thiourea (PTU) was added to the culture water to inhibit pigment expansion in the zebrafish.

Zebrafish larvae were stochastically divided into three groups ($n=30$): the control, AuNP, and EA-AuNP groups. Under a stereo microscope (SZX7, OLYMPUS, Japan), 4 dpf zebrafish were fixed with 1.5% low melting point adhesive, and then 5 nL of 0.5 mg/mL EA-AuNP or AuNP solution was injected. For each live imaging time point (0 hpf, 24 hpf, 48 hpf, and 72 hpf), five randomly selected zebrafish were imaged using a laser confocal microscope (AX, Nikon, Japan) in reflection mode. ImageJ software was employed to quantify the integrated density of the obtained images.

In vivo micro-CT scanning imaging

In vivo micro-CT scanning imaging was conducted using a micro-CT scanner (Skyscan 1176, Bruker Micro-CT, Kontich, Belgium) with the following parameters: X-ray source voltage, 60 kV; X-ray source current, 385 μA; camera pixel, 12.28 μm; rotation range, 180 degrees; rotation step, 0.7 degrees; and exposure time, 50 ms. Mice were anesthetized with pentobarbital sodium prior to the in vivo imaging experiments. Subsequently, 0.4 mL of EA-AuNPs (50 mg/mL, dispersed in deionized water)

was injected intravenously into the mice. Micro-CT scans were performed at 2 h, 72 h, and 120 h post the EA-AuNP injection. After imaging, mice were sacrificed, and the heart, liver, kidney, spleen, and intestine were re-imaged using micro-CT. The raw data were analyzed using DataViewer, and 3D rendering images were obtained by CTvox.

In vitro oxidative stress assay

The protective effects of EA-AuNPs on H9c2 cells in an oxidative stress microenvironment were investigated [27]. H9c2 cells were seeded in 96-well plates at a density of 1×10^4 cells/well. After 24 h, the culture medium of H9c2 cells was replaced with fresh medium containing EA-AuNPs and co-incubated for 6 h. After that, the culture medium was removed, and H9c2 cells were treated with various concentrations of H_2O_2 and co-incubated for an additional 12 h. Cell viability was determined by MTT assay, and the morphology of H9c2 cells was visualized using optical microscopy. A lactate dehydrogenase (LDH) assay kit was used to detect LDH activity in the collected culture medium.

H9c2 cell apoptosis assay

An Annexin V/7-AAD apoptosis kit and a Hoechst 33,258 staining kit were used to investigate the protective effect of EA-AuNPs on the H_2O_2-induced cardiomyocyte apoptosis. Following treatment with EA-AuNPs and stimulation with H_2O_2, H9c2 cells were collected and sequentially treated with FITC Annexin V and 7-AAD. After washing with PBS, the number of apoptotic cardiomyocytes was measured by flow cytometry. Additionally, H9c2 cells were fixed and stained with Hoechst 33,258 staining solution, and the slides were observed and photographed under an inverted fluorescence microscope.

Intracellular ROS detection

A DCFH-DA probe was employed to detect the intracellular ROS levels in H_2O_2-induced apoptotic cardiomyocytes. After treatment with EA-AuNPs and stimulation with H_2O_2, H9c2 cells were incubated in a serum-free culture medium containing DCFH-DA for 20–30 min. The positive control group was stimulated with the ROS positive control reagent Rosup. After washing with PBS, the cells were detected by a flow cytometer at an excitation wavelength of 488 nm and an emission wavelength of 525 nm.

Cellular oxidative stress indicators detection

Oxidative stress levels in H_2O_2-induced cardiomyocytes were strictly measured using commercial assay kits for superoxide dismutase (SOD), glutathione peroxidase (GSH-Px), and malondialdehyde (MDA), along with ultraviolet and visible spectrophotometry (UV−Vis).

Cellular lipidomics analysis

After EA-AuNP treatment and H_2O_2 stimulation, H9c2 cells (approximately 1×10^7 cells) were collected, washed with precooled PBS, and then centrifuged at 800 rpm for 5 min at 4 °C. Subsequently, precooled ultrapure water was added, followed by sufficient homogenization. The lipids were extracted using a modified Bligh and Dyer method [28]. The protein concentration of the cells was determined according to the instructions of the bicinchoninic acid (BCA) assay kit. Then, 1.2 mL of $CHCl_3$/MeOH (2:1, v/v), 0.3 mL of ultrapure water, lipid internal standards, and 10 μL of BHT solution were added to the homogenized samples. The obtained mixture was subjected to ultrasound-assisted extraction for 5 min to release the lipids from the solid matrix, followed by centrifugation at 15,000 rpm for 10 min at 4 °C. The upper and lower phases were collected separately, vortexed, and centrifuged again after adding 0.6 mL of $CHCl_3$. The organic phase was collected and evaporated under a nitrogen stream.

Cellular lipid separation was performed on an Agilent 1290 Infinity II LC system (Agilent Technologies, Waldbronn, Germany) equipped with an Agilent ZORBAX Eclipse Plus C18 (100×2.1 mm, 1.8 μm, Agilent) column. The gradient elution program consisted of mobile phase A (MeOH/ACN/water, 1:1:1, v/v/v) and mobile phase B (ACN/IPA, 1:5, v/v) with the following gradient profile: 0–0.5 min, 20% B; 0.5–1.5 min, 40% B; 1.5–3 min, 60% B; 3–13 min, 98% B; 13–17 min, 20% B. The flow rate was set at 0.4 mL/min. The injection volumes for both negative and positive modes were 2 μL. For MS/MS detection using 6560 Q-TOF (Agilent Technologies, Waldbronn, Germany), the capillary voltages were set at 3500 V and −3500 V for the two modes, The gas temperature 350 °C, nebulizer gas 35 psi, drying gas 8 L/min, and mass range 200–1200 Da. The MS/MS data acquisition process was carried out using the data dependent acquisition (DDA) mode.

Induction of the mouse MI model

C57BL/6J mice (male, weighing approximately 20 g) were bought from Jiangsu GemPharmatech Co., Ltd. (China). The local Animal Ethics Committees of the State Key Laboratories for Quality Research in Chinese Medicines, Macau University of Science and Technology approved all the animal studies (Approved number: 072/DICV/DIS/2021). The experimental MI model was induced by administering intraperitoneal injections of isoproterenol HCl (ISO) (150 mg/kg b.w.) on two consecutive days (days 8 and 9), with a 24-hour interval between injections. The animal experiment lasted for 9 days. Mice were stochastically divided into five groups ($n=10$ each): control, ISO, AuNPs (100 mg/kg b.w.)+ISO, L-EA-AuNPs (100 mg/kg b.w.)+ISO, and H-EA-AuNPs (200 mg/kg

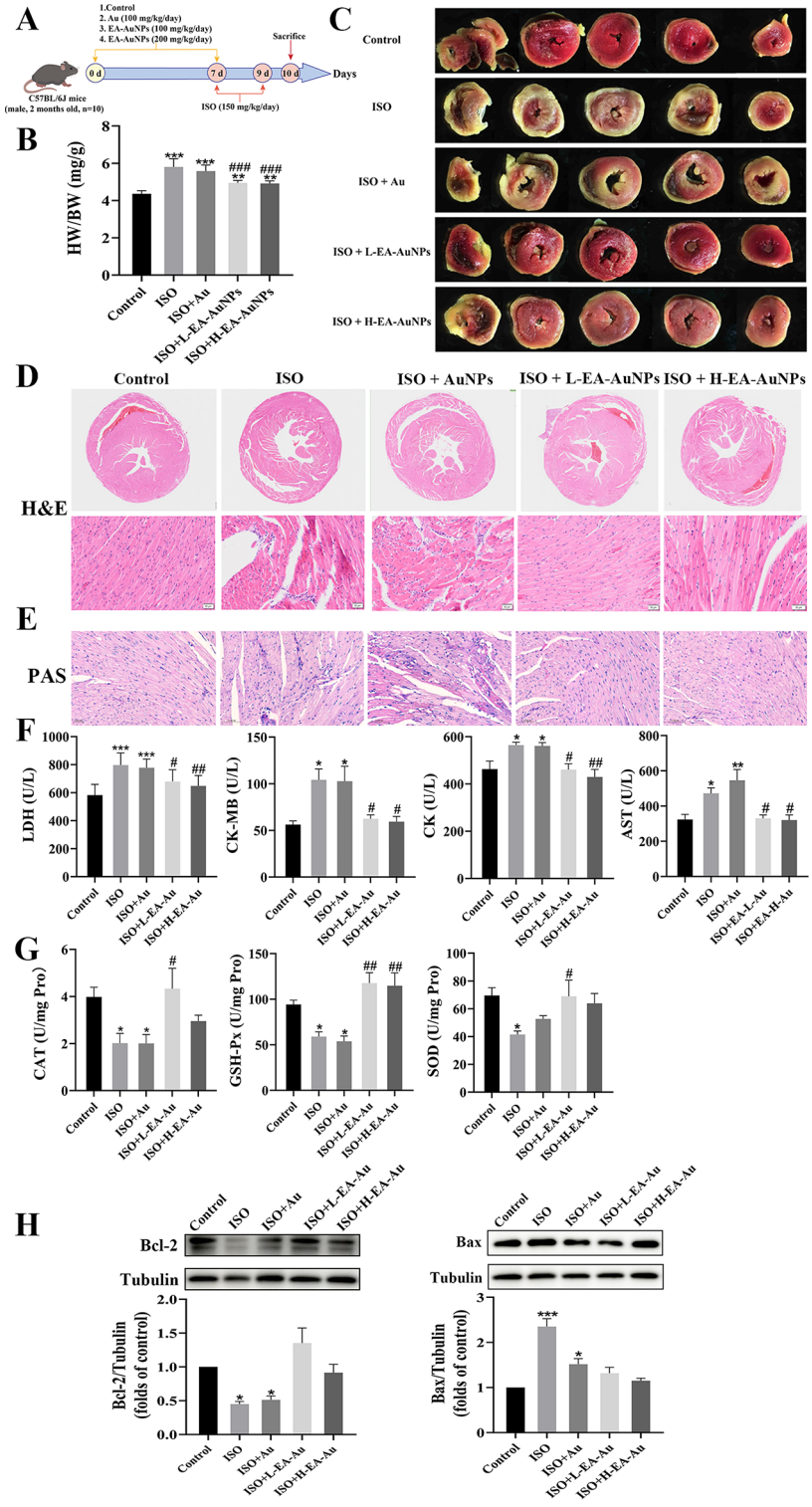

Fig. 4 EA-AuNP treatment ameliorated MI injury in mice. (**A**) Schematic illustration of the experimental design. (**B**) The ratio of heart weight to body weight in MI mice. (**C**) Representative images of TTC-stained cardiac sections. (**D**) H&E staining of cardiac sections in differenr groups (scale bar = 50 μm). (**E**) PAS staining of cardiac sections in differenr groups (scale bar = 20 μm). (**F**) Effects of EA-AuNP treatment on the levels of the cardiac marker enzymes LDH, CK-MB, CK, and AST. Lactate dehydrogenase: LDH; creatine kinase MB isoenzyme: CK-MB; creatine kinase: CK; aspartate aminotransferase: AST. (**G**) Effects of EA-AuNP treatment on oxidative damage in MI mice. (**H**) Protein expression levels of Bcl-2 and Bax in differenr groups. Values are mean ± SEM ($n = 6$); $^{**}p < 0.01$, $^{***}p < 0.001$ vs. control group; $\#\#p < 0.01$, $\#\#\#p < 0.001$ vs. ISO group

b.w.)+ISO. AuNPs and EA-AuNPs were injected intraperitoneally for 7 consecutive days before the MI induction. All mice were sacrificed on the 10th day following MI induction. The heart was weighed, and the heart-to-body weight ratio was calculated. A portion of the heart was immediately subjected to TTC staining, while the remainder was stored at -80 °C for further analysis. A schematic illustration of the experimental design is shown in Fig. 4A.

Histology

Heart tissues were fixed in 10% formalin overnight, then embedded in paraffin. The 5 μm slices were stained with hematoxylin-eosin (H&E) and periodic acid–Schiff (PAS) for histopathological examination and glycogen detection.

Detection of myocardial enzymes and serum redox indexes

After being left at room temperature for 30 min, the collected mouse blood was centrifuged at 3000 rpm for 10 min. The serum levels of LDH, creatine kinase (CK), creatine kinase MB isoenzyme (CK-MB), aspartate aminotransferase (AST), and nitric oxide (NO) were measured using assay kits obtained from Nanjing Jiancheng Bioengineering Institute (Jiangsu, China). The activities of catalase (CAT), SOD, and GSH-PX in cardiac tissue were also detected using assay kits following the manufacturer's instructions.

Western blot

Western blot analysis was conducted to evaluate the expression of apoptosis-related proteins. Isolated hearts were homogenized in RIPA lysis buffer containing protease inhibitor cocktail (Sigma Aldrich) and centrifuged at 12,000 rpm for 10 min. The total protein content was confirmed by a BCA assay kit. Proteins (30 μg) were electrophoresed and separated via 12% SDS–PAGE, transferred to PVDF membranes, and then blocked in a 5% skim milk solution. The membrane was incubated with the following primary antibodies: Bcl-2, Bax, and caspase-3 (all at 1:1000; Cell Signaling Technology, USA). The blots were visualized with an Amersham ImageQuant 800 and measured using ImageJ software.

Serum oxylipin profile analysis

An aliquot of serum (50 μL) containing deuterated standards was dissolved in 1 mL of methanol/water (v/v, 1:9) solution and subjected to ultrasound-assisted extraction at 4 °C for 30 min. The extracts were then purified and enriched by Strata-X reversed-phase solid-phase extraction (SPE) cartridges. The eluate was collected and evaporated under a nitrogen stream. Before detection, the samples were reconstituted with 100 μL of methanol/water (v/v, 1:1) solution and centrifuged at 10,000 rpm. The supernatant was then collected for oxylipin profile analysis.

Serum levels of oxylipins were identified and quantified using HPLC-MS/MS, as described previously [29]. Chromatographic separation was performed on an Agilent 1260 HPLC system (Agilent Technologies, Waldbronn, Germany) equipped with a C18 column (4.6×100 mm, 1.8 μm, Agilent). The gradient elution program was composed of mobile phase A (ACN/water/acetic acid (60:40:0.02, v/v/v)) and mobile phase B (ACN/IPA (50:50, v/v)) with the following gradient profile: 0–4 min, 55% B; 4–15 min, 55-99% B; 15–16 min, 99% B; and 16–18 min, 99%-55% B. The flow rate was set at 0.4 mL/min. The injection volume was 5 μL. Following the separation, the parameters were reset to the starting point for equilibration, and the column was washed.

A 6495 C QQQ mass spectrometer (Agilent Technologies, Waldbronn, Germany) with scheduled multiple reaction monitoring (MRM) was used for MS detection. The electrospray voltage and gas temperature were set at 3500 V and 350 °C, respectively. The nebulizer gas was set at 20 psi, and the sheath gas temperature was 200 °C. The stable isotope as internal standards (IS) served as the basis for the quantification of oxylipins.

Statistical analysis

All experimental data with error bars are presented as the mean±SEM. Differences between the two groups were assessed by one-way analysis of variance (ANOVA) using GraphPad Prism 9 software. A value of $p<0.05$ was denoted statistically significant.

Results and discussion

Synthesis of AuNPs using polyphenols

The ratio of reductant to gold precursor is crucial in the nucleation of AuNPs. Therefore, we optimized the synthesis of the gold-phenolic core-shell nanoparticles by varying the concentration of the $HAuCl_4$ solution and confirmed the ideal concentration for the rapid formation of AuNPs based on surface plasmon resonance (SPR) absorption band analysis. The UV-Vis spectra, as a function of $HAuCl_4$ solution concentration, for the synthesized AuNPs using epicatechin, catechin, taxifolin, gallic acid, and ellagic acid are depicted in Fig. 1A. All five AuNPs showed an SPR band ranging from 540 to 570 nm at appropriate concentrations, which is consistent with the characteristic absorption peaks of AuNPs reported previously [30, 31]. The absorbance spectra initially demonstrated that these five compounds could serve as effective natural reductants for synthesizing AuNPs without the need for other hazardous chemicals. While maintaining the concentration and volume of the phenolic compound solution constant, the gold precursor concentration had a significant concentration-dependent impact

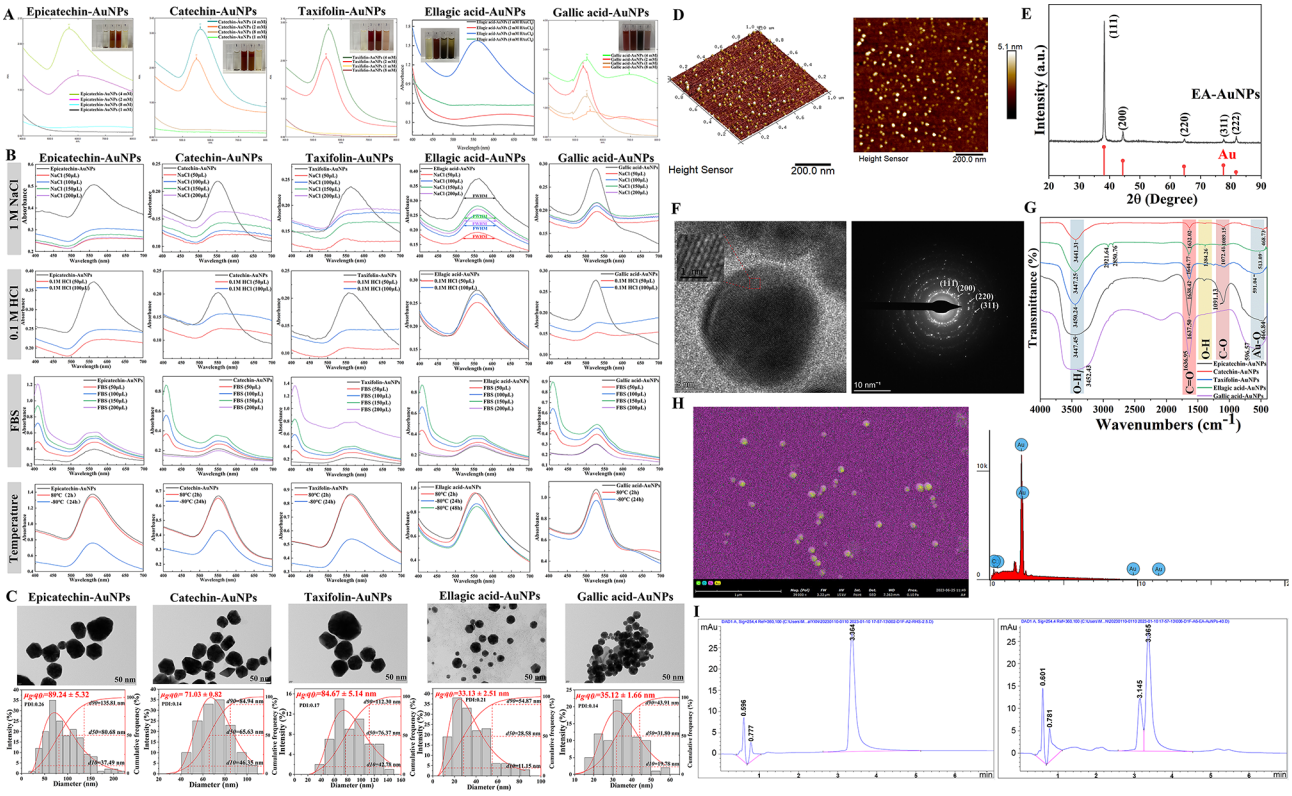

Fig. 1 Preparation and characterization of gold-phenolic core-shell nanoparticles. (**A**) UV-Vis absorption spectra of five gold-phenolic core-shell nanoparticles showing the effect of $HAuCl_4$ concentration. (**B**) UV-Vis spectra showing the effect of different temperatures and volumes of 0.1 M NaCl, 1 M NaCl, and FBS on the stability of five gold-phenolic core-shell nanoparticles. (**C**) TEM images and TEM size distribution histogram of optimized gold-phenolic core-shell nanoparticles. (**D**) 2-dimensional images and 3-dimensional AFM images of the EA-AuNPs. (**E**) XRD spectra of Au and EA-AuNPs. (**F**) HR-TEM images and SAED patterns of the EA-AuNPs. (**G**) FT-IR spectra of gold-phenolic core-shell nanoparticles. (**H**) Elemental analysis of EA-AuNPs. (**I**) HPLC chromatograph of the ellagic acid standard (2.5 μg/mL, left) and supernatant (right) obtained after the reaction of ellagic acid and chloroauric acid

on the synthesis process. The absorbance intensity of the SPR peak increased for the $HAuCl_4$-reductant ratio from 1:5 to 4:5 and decreased with the SPR peak disappearing at a ratio of 8:5. This result indicates that a relatively high concentration of reductant may affect the growth of nanoparticles.

Stability evaluation

The stability of new nanomaterials is a crucial factor for their successful biomedical applications [32], as only highly stable nanoparticles can effectively tolerate severe biological environments to maximize their therapeutic efficacy across different diseases [33, 34]. To assess the stability, we selected the optimum concentration of gold precursor solution for each type of gold-phenolic core-shell nanoparticle based on the absorbance intensity. EA-AuNPs demonstrated excellent stability during a 2 h incubation in both FBS and 0.1 M HCl solutions. Furthermore, their stability was superior to that of other AuNPs in a 1 M NaCl solution, as indicated by the absence of shift in their SPR peaks and the essentially constant full width at half maximum (FWHM) values (Fig. 1B). In contrast, the other four types of gold-phenolic core-shell nanoparticles exhibited progressive broadening of their absorption peaks, which vanished entirely in different solutions, indicating a total loss of structural integrity. Moreover, once the storage temperature was decreased to -80 ℃, minimal intensity changes (<10%) were observed for the EA-AuNPs and gallic acid-AuNPs compared to their absorbance at room temperature, while a roughly 40% reduction in the characteristic SPR intensity was found for the other three types of gold-phenolic core-shell nanoparticles. In summary, the EA-AuNPs exhibited exceptional stability in various environments, showing no discernible agglomeration in the solution. All these stability assessments demonstrated that the EA-AuNPs have medical robustness and applicability for further experiments. Therefore, we characterized and conducted in vitro and in vivo studies on the EA-AuNPs.

Characterization of the EA-AuNPs

TEM and AFM were used to characterize the surface micromorphology, shape, and size of the gold-phenolic core-shell nanoparticles (after multiple washes), which presented a uniform quasi-nearly spherical shape with a relatively smooth surface (Fig. 1C and D). The particle

diameters of the EA-AuNPs and gallic acid-AuNPs were smaller than those of the other three materials. The corresponding Gaussian fitting curve indicates that the nanoparticle core of the EA-AuNPs mainly ranges from 20 nm to 40 nm in diameter. The fluctuation in the particle size distribution may be determined by the amount of ellagic acid molecules linked to the nanoparticles. As shown in Fig. S2, the synthesized EA-AuNPs have an encircling light gray layer, indicating a thin organic covering on the surface; the shell thickness was 4±1 nm. The X-ray diffraction (XRD) patterns confirmed the face-centered cubic (fcc) structure of the EA-AuNPs [35]. As depicted in Fig. 1E, the diffraction pattern of the EA-AuNPs shows five distinct diffraction peaks that are satisfactorily accredited to those in the pure Au crystal phase (JCPDS card: File No. 04–0784) [36]. Moreover, the high-resolution TEM (HR-TEM) image revealed clear lattice stripes of the EA-AuNPs, confirming their uniform thickness and crystalline characteristics (Fig. 1F). The lattice spacing of the EA-AuNPs was 0.21 nm, which corresponds to the (111) planes of Au. The HR-TEM-based SAED pattern showed several well-dispersed diffraction rings resulting from reflections of lattice planes [37]. The spots in the diffraction rings, corresponding to different orientations of Au, also demonstrated the crystalline structure of the EA-AuNPs.

The successful doping of ellagic acid with AuNPs was confirmed by FT-IR and EDS analyses. As shown in Fig. 1G, all types of AuNPs exhibited similar patterns of absorption peak changes in the infrared regions before and after the synthesis. Taking EA-AuNPs as an example, when comparing the FT-IR data with that of the ellagic acid standards, the intensity of the absorption bands related to the hydroxyl groups (–OH) significantly decreased in the EA-AuNPs' FT-IR spectra, indicating that the –OH groups of ellagic acid were involved in the formation of the AuNPs. Additionally, the shifts in the characteristic peaks of ellagic acid from 1619.9 cm^{-1} to 1644.8 cm^{-1} and 1057.1 cm^{-1} to 1072.4 cm^{-1} indicated that the absorption band of the carbonyl group also shifted in the spectrum of the EA-AuNPs. The above results demonstrated that the hydroxyl groups of ellagic acid may have been oxidized into carbonyl groups through hydrogen bonding interactions during the chemical reduction of Au^{3+} to Au^{0} [38]. As shown in the EDS spectrum of the EA-AuNPs (Fig. 1H), a strong signal peak at 2.3 keV is indicative of the characteristic X-ray emission from metallic gold (Au) nanocrystallites, the minor peaks at 0.2 keV and 0.5 keV also indicate the presence of carbon and oxygen. The elemental mapping in Fig. 1H illustrates the distribution of carbon (green) and oxygen (blue) elements on the surface of the EA-AuNPs, implying the successful involvement of ellagic acid in the synthesis of AuNPs.

Assembly efficiency of ellagic acid in EA-AuNPs

To further elucidate the assembly efficiency of ellagic acid in EA-AuNPs, we detected the concentration of ellagic acid in the supernatant of EA-AuNPs after synthesis and centrifugation using UHPLC. One of the most crucial properties of nanoparticle-based drug delivery systems is the drug loading efficiency, which determines the therapeutic effect [39]. Based on the peak areas of the characteristic ellagic acid peak shown in Fig. 1I (left), the concentration of this compound was estimated using the standard curve. Under optimal synthesis conditions, the initial total concentration of the ellagic acid solution used in the synthesis process was 1.2 mg/mL, and the concentration of free ellagic acid in the supernatant of the EA-AuNPs was 82.8 μg/mL. Therefore, the assembly efficiency of ellagic acid was calculated to be 93.1%, indicating that ellagic acid is almost entirely assembled in AuNPs.

In vitro biocompatibility study of the EA-AuNPs

Evaluating the potential cellular toxicity of nanomaterials is crucial for assessing their biocompatibility in in vivo experiments and biomedical applications. In vitro cytotoxicity assays were conducted on both EA-AuNPs and AuNPs using the THP-1 and H9c2 cell lines. Fig. 2A shows that AuNPs exhibited a significant dose-dependent inhibitory effect on cell viability as the concentration increased from 50 μg/mL to 800 μg/mL. Additionally, at the same concentrations, AuNPs exerted pronounced cytotoxic effects on activated THP-1 cells compared with H9c2 cells, with a 50% reduction in cell viability observed at 800 μg/mL. Conversely, the cell viability results for the EA-AuNP groups indicated that both cell lines maintained high viability after 24 h of incubation. Even at the highest concentration of 800 μg/mL, no cytotoxicity was observed in cells co-incubated with EA-AuNPs. Annexin V-FITC/7-AAD double-staining assays on both cell lines treated with EA-AuNPs also showed negligible percentages of apoptotic cells compared to the control group (Fig. 2B).

Oxidative stress-mediated cell apoptosis is an essential mechanism of cytotoxicity associated with AuNP exposure. Therefore, we evaluated the ROS generation in activated THP-1 and H9c2 cells co-incubated with EA-AuNPs for 24 h to confirm whether they contribute to oxidative stress. The intracellular ROS levels in these two cell lines showed minimal green fluorescence in both the control group and the EA-AuNP-treated group, even at the highest nanoparticle concentration, aligning with the results of the cytotoxicity assays (Fig. 2C). Notably, the ROS fluorescence intensity peaks of H9c2 and THP-1 cells treated with EA-AuNPs gradually shifted to the left with increasing nanoparticle concentration, indicating that the EA-AuNPs could reduce the intracellular ROS

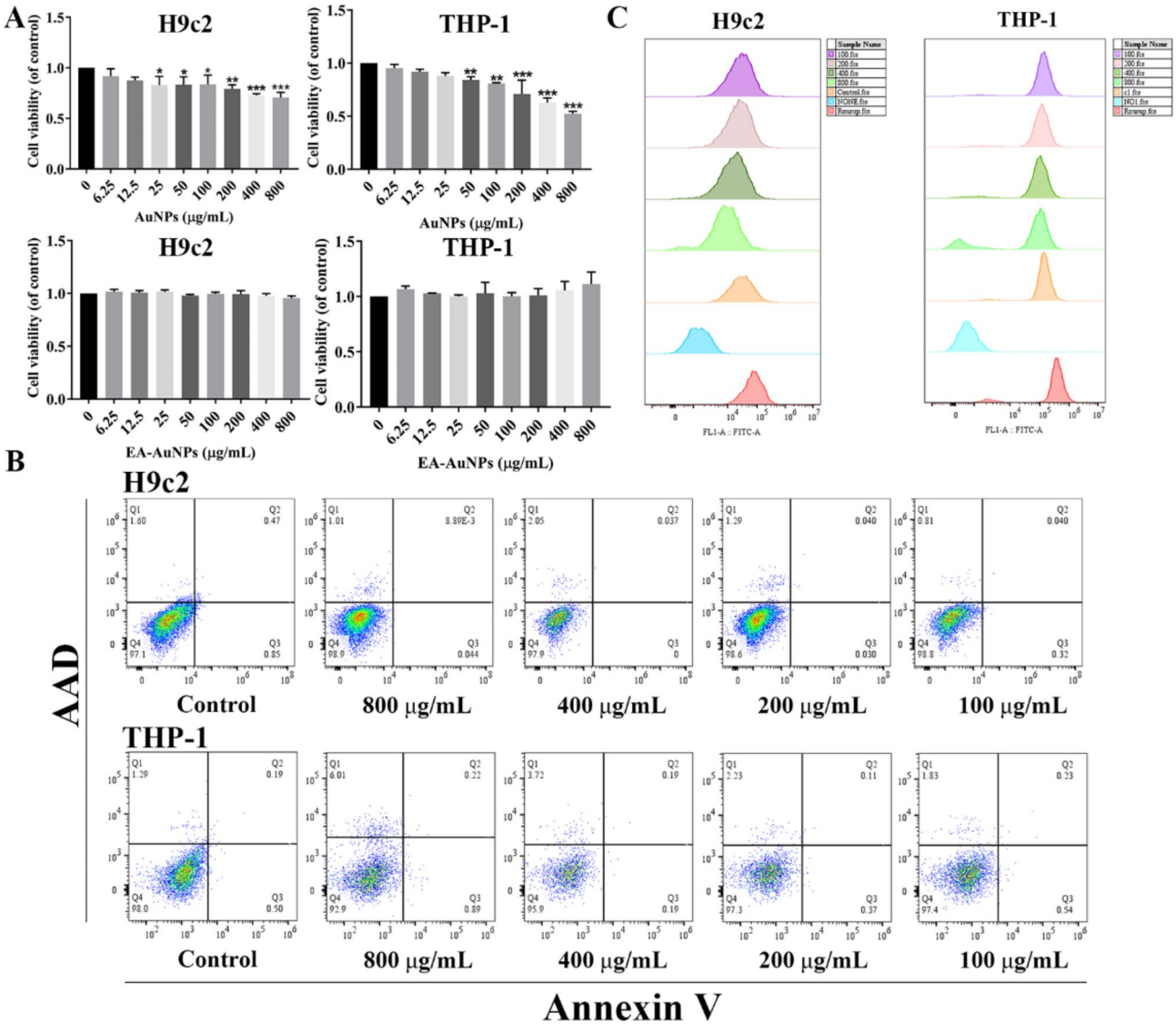

Fig. 2 Biocompatibility of the EA-AuNPs assessed in vitro. (**A**) In vitro cytotoxicity of different concentrations of AuNPs and EA-AuNPs (0–100 μg/mL) for 24 h. (**B**) Intracellular ROS levels in H9c2 and THP-1 cells treated with different concentrations of EA-AuNPs for 24 h. (**C**) Evaluation of H9c2 and THP-1 cell apoptosis after treatment with different concentrations of EA-AuNPs for 24 h. Values are mean ± SEM ($n = 6$); $^{*}p < 0.05$, $^{**}p < 0.01$, $^{***}p < 0.001$ vs. control group

levels. In summary, compared with AuNPs, EA-AuNPs do not elicit cytotoxicity, making them suitable for biomedical applications.

Bioaccumulation and clearance of EA-AuNPs

The bioaccumulation and elimination of nanoparticles in living organisms are always under investigation, which is pivotal for their development and translation in clinical applications [40, 41]. Many functional nanoparticles lack the ability to emit fluorescence, and fluorescent groups linked to their surface can easily separate in vivo, often producing misleading results. Therefore, we developed a label-free imaging method, in combination with the use of optically transparent zebrafish larvae models, to precisely visualize bioaccumulation patterns and quantify EA-AuNPs in vivo. As illustrated in the schematic (Fig. 3A), EA-AuNPs and AuNPs were injected into 4 dpf zebrafish larvae, followed by imaging at 0, 1, 2, and 3 days post-injection (dpi) using a laser confocal microscope under reflection mode. As shown in Fig. 3B, the bioaccumulation of EA-AuNPs in the zebrafish was clearly observed at 2 h post-injection, while the tiny particle size of the AuNPs rendered them undetectable, confirming the applicability of this non-invasive and label-free imaging method for EA-AuNP detection in zebrafish. The large amount of reflected light in the zebrafish larvae at 0 dpi indicates that the EA-AuNPs were widely distributed throughout the organism. After 20 h of in

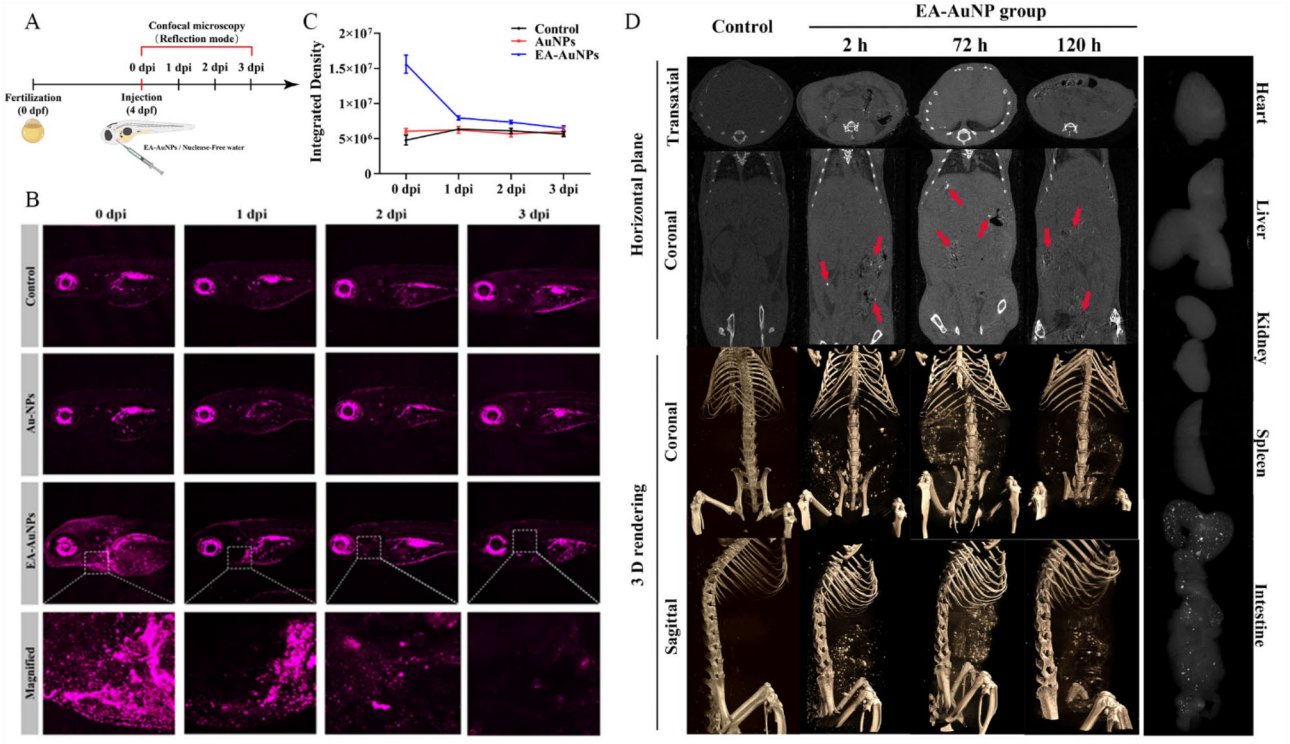

Fig. 3 Bioaccumulation pattern and metabolic route of EA-AuNPs in zebrafish and mouse models. (**A**) Schematic illustration of the experimental design for the bio-distribution exploration of EA-AuNPs in zebrafish. (**B**) Histogram of reflection signal analysis of zebrafish after EA-AuNP and AuNP injection (images were acquired at 0 dpi, 1 dpi, 2 dpi, and 3 dpi). (**C**) Confocal laser scanning microscopy (CLSM) images (reflection mode) of zebrafish injected with EA-AuNPs. (**D**) In vivo serial CT images of mice after intravenous injection of EA-AuNPs (images were acquired at 2 h, 72 h, and 120 h). The CT signals are indicated with the red arrow

vivo circulation, the amount of reflected light noticeably declined, suggesting substantial clearance of the EA-AuNPs in the zebrafish. The integrated density of the reflected light was further quantified to assess the elimination time of EA-AuNPs in zebrafish (Fig. 3C). Quantitative reflection light analysis showed that the content of EA-AuNPs decreased dramatically after 24 h and then decreased progressively over time since injection. At 3 dpi, the quantified values of reflection light in the EA-AuNP group approached those of the control group, indicating the successful excretion of most EA-AuNPs from the zebrafish. The results from the zebrafish experiments confirmed the low accumulation of EA-AuNPs in vivo.

It is challenging to observe the specific metabolic route of these nanoparticles in zebrafish. To non-invasively monitor the in vivo metabolic route of EA-AuNPs, we injected mice with 0.4 mL of EA-AuNPs (50 mg/mL, dispersed in deionized water) and imaged them at different time points using micro-CT. As shown in CT images, soft tissues appeared gray or dark, while bones and EA-AuNPs appeared white due to their higher density and, thus, increased X-ray absorption. Real-time micro-CT images acquired from the coronal and transaxial planes showed enhanced CT signals in the middle and rear parts of the mice at 2 h post-injection. The CT signals from various parts of the mice indicated that the EA-AuNPs were circulating within the mice's bodies. The barely visible signal in the upper region of the mice indicated a low accumulation of EA-AuNPs in the mouse heart and lungs. At 3 days post-injection, CT signals remained, primarily concentrated around the intestines, indicating the uptake of EA-AuNPs by these organs. Three-dimensional rendering of CT images was employed to investigate the bioaccumulation and migration of EA-AuNPs in the mice. As depicted in Fig. 3D, EA-AuNPs were widely distributed in the intestines of mice for a relatively long time, with the intensity and amount of CT signals progressively decreasing over time, potentially indicating excretion. Subsequently, at 5 days post-injection, fewer CT signals were captured in other organs, indicating that the metabolic route of the EA-AuNPs predominantly involved the intestines. Therefore, after imaging, we euthanized and dissected the mice to further confirm the metabolic route of the EA-AuNPs. The ex vivo CT imaging of the main metabolic organs revealed the presence of signals in the liver, spleen, and intestines (Fig. S3). Moreover, the intensified CT signals in the intestines suggest a substantial aggregation of EA-AuNPs in the large intestine. An examination of feces obtained from the large intestine of the mice, which displayed a distinctive golden color,

confirmed the excretion of EA-AuNPs. We hypothesize that after EA-AuNPs are injected via the tail vein into mice, they enter the small intestine through the enterohepatic circulation, subsequently accumulate in the large intestine (evidenced by the prominent CT signal), and ultimately are excreted in the feces, aligning with the previous investigations of AIE active quercetin nanocrystals [42]. In conclusion, EA-AuNPs possess many advantages, including a comparatively lengthy intestinal retention period with minimal impact on other organs and satisfactory excretion-based metabolism.

In vivo therapeutic efficacy of EA-AuNPs in MI mice

Ellagic acid, a bioactive polyphenol predominantly present in hydrolyzable tannin forms within a variety of berries and nuts, has garnered considerable attention for its multifaceted biological activities [43]. The compound has been extensively documented for its capacity to inhibit lipid peroxidation, exert anti-inflammatory responses, mitigate atherosclerotic processes, and demonstrate potent antioxidant and anti-apoptotic effects [44, 45]. Recent research further supports the protective role of ellagic acid against isoproterenol-induced arrhythmias, myocardial infarction, and cardiac fibrosis, primarily attributed to its enhanced free radical scavenging capabilities [46]. The intrinsic chemical structure of ellagic acid, characterized by the presence of four hydroxyl groups and two lactone moieties, endows it with an exceptional propensity to trap free radicals through electron donation. However, this molecular structure, incorporating both lipophilic and hydrophilic domains, imposes constraints on its clinical applicability [47]. While the amphiphilic nature of ellagic acid is beneficial for its antioxidant activity, it also presents challenges in terms of bioavailability, solubility, and formulation stability—factors that are pivotal for pharmaceutical development and efficacy. Advancements in nanotechnology have emerged as a promising way to overcome the aforementioned challenges. Specifically, the application of nanotechnology has the potential to enhance the bioavailability and solubility of ellagic acid, thereby mitigating its inherent physiochemical limitations and reducing the propensity for adverse toxicological effects [48, 49]. Motivated by the results of a biocompatibility study suggesting the potential antioxidant ability of EA-AuNPs, we next investigated the protective efficacy of EA-AuNPs in an ISO-induced MI mouse model [50]. The ratio of heart weight to body weight (HW/BW) is commonly used to assess cardiac hypertrophy [51]. Compared to the control groups, the HW/BW index showed a significant increase in the ISO and AuNP groups ($p<0.0001$), while both low- and high-dose EA-AuNP treatments inhibited this increase (Fig. 4B). As an intuitive indicator of myocardial injury, myocardial infarct size was visualized using 2,3,5-triphenyl tetrazolium chloride (TTC) staining, where the infarct area appears as a yellow-white color. In the ISO and AuNP groups, a series of TTC-stained heart slices showed a prominent increase in myocardial infarct size (Fig. 4C). Remarkably, EA-AuNP treatment reduced the infarct area in ISO-administered mice, and the yellow-white region was almost invisible in both EA-AuNP treatment groups, similar to that in the control group. H&E staining of whole-heart images showed a thinner left ventricular wall and an expanded left ventricular chamber in both the ISO and AuNP groups and EA-AuNP treatment notably inhibited these pathological changes (Fig. 4D). Magnified images revealed typical morphological damage, including inflammatory cell infiltration, disordered myocardial fibers, and cytoplasmic vacuolar degeneration, in the ISO and ISO + AuNP groups. Conversely, low- and high-dose EA-AuNP treatment markedly ameliorated these symptoms, presenting a complete myocardial structure and clear nucleus structure. In addition, we used PAS staining to evaluate the glycogen deposition in the myocardium, which is predominantly characterized by a purplish-red color in PAS-positive reactions. PAS staining showed mild glycogen deposition in the myocardium of the ISO group and increased glycogen deposition in the myocardium of the AuNP group (Fig. 4E). Treatment with EA-AuNPs ameliorated the glycogen deposition, indicating that EA-AuNPs alleviated the impairment of glucose metabolism in ISO-administered mice.

Then, we measured the activities of several cardiac enzymes in the serum, including LDH, CK-MB, CK, and AST, to investigate the bioactive impact of EA-AuNPs in ISO-administered mice. These enzymes, known as the main diagnostic biomarkers for MI, exhibited significantly elevated activity levels in both the ISO and AuNP groups (Fig. 4F). Conversely, EA-AuNPs inhibited the ISO-induced increase in cardiac enzyme activity.

MI disrupts the intracellular redox state (i.e., an imbalance in the production and removal of reactive oxygen species), resulting in myocardial damage and cardiac remodeling. To verify whether the bioactive effect of EA-AuNPs stems from their antioxidant activity, we further examined several typical indicators reflecting the extent of oxidative stress in ISO-administered mice. As shown in Fig. 4G, compared to those in the control group, the activity levels of CAT, GSH-PX, and SOD decreased in both the ISO and AuNP groups, whereas treatment with low- and high-dose EA-AuNPs markedly reversed these conditions in varying degrees. In particular, L-EA-AuNP treatment notably enhanced the activities of CAT, GSH-PX, and SOD to normal levels. These results indicated that EA-AuNP treatment could improve the antioxidant activity of cardiomyocytes to counteract oxidative damage.

To further confirm the cardioprotective effect of EA-AuNP treatment, we also assessed the expression of apoptosis-related proteins in cardiac tissues. Both the anti-apoptotic protein Bcl-2 and the pro-apoptotic protein Bax were evaluated in cardiac tissues with or without EA-AuNP treatment. As shown in Fig. 4H, various doses of EA-AuNPs significantly elevated the expression of Bcl-2 and decreased the expression of Bax, indicating reduced apoptosis. Specifically, treatment with low and high doses of EA-AuNPs resulted in a 1.8- and 2.0-fold decrease in the expression of Bax, and a 3.0- and 2.0-fold increase in the expression of Bcl-2, respectively, compared to those in ISO-induced mice. Collectively, these results demonstrate that EA-AuNP treatment prevents MI-induced cardiac injury by downregulating apoptosis.

Anti-apoptosis and ROS scavenging abilities of EA-AuNPs in cardiomyocytes

Additional in vitro investigations were conducted to gain further insights into the cardioprotective effects of EA-AuNP treatment. High levels of ROS are generated by tissue damage in MI, leading to oxidative stress and cell apoptosis, with H_2O_2 as a major constituent of ROS [52]. Therefore, a cellular oxidative stress model in H9c2 cells was constructed under H_2O_2 stimulation [53]. As depicted in Fig. 5A, the cell viability declined by almost 50% after treatment with 400 μM H_2O_2, approaching the half-maximal inhibitory concentration (IC50). Therefore, we selected 400 μM H_2O_2 for the following experiments. Fig. 5B shows that treatment with 500 μg/mL EA-AuNPs obviously ameliorated the cytotoxic effects on H9c2 cells after H_2O_2 stimulation, resulting in increased cell viability.

H_2O_2 treatment led to incomplete cell membrane structure and shrunken cell morphology. Conversely, EA-AuNP treatment protected H9c2 cells against H_2O_2-induced morphological changes. The results of Annexin V/7-AAD flow assays also indicated that EA-AuNP treatment significantly reduced the proportion of apoptotic cells (1.47 ± 0.69% early and 0.31 ± 0.20% late apoptotic cells), resembling the levels observed in the control group (Fig. 5C). We also confirmed that treatment with 800 μg/mL AuNPs, obtained by the sodium citrate reduction process, failed to reduce the number of H_2O_2-induced apoptotic cells (Fig. S4). Typical fluorescence microphotographs from the Hoechst 33,258 experiment showed the fragmented nuclei and chromatin condensation (indicated by white arrows) in H9c2 cells after H_2O_2 treatment, however, these typical morphological changes were not observed in the EA-AuNP groups (Fig. 5D).

The H_2O_2-induced oxidative stress environment generates excessive ROS, which can cause cellular dysfunction, eventually leading to cell death and severe inflammation [54]. Flow cytometry analysis showed markedly increased levels of intracellular ROS in cells exposed to H_2O_2, while treatment with 800 μg/mL EA-AuNP significantly inhibited ROS production in cardiomyocytes, as evidenced by the left-shifted fluorescence intensity peaks (Fig. 5E). Further quantification of the mean fluorescence intensity confirmed the potent antioxidant capacity of the EA-AuNPs. We also demonstrated that the antioxidant ability of EA-AuNPs is not mediated by the AuNPs themselves but may be attributed to the bioactivity of ellagic acid (Fig. S5) [55].

Under oxidative stress conditions, cardiomyocyte injury can be assessed by detecting lactate dehydrogenase (LDH) release. LDH release assays showed that EA-AuNP treatment had a marked inhibitory effect on LDH leakage, which was reduced to 77% ± 6.07% of that in the control group (Fig. 5F). We also further detected several intracellular oxidative stress markers, including superoxide dismutase (SOD), glutathione peroxidase (GSH-Px), and malondialdehyde (MDA), to evaluate the antioxidant abilities of the EA-AuNPs [56, 57]. The activities of endogenous antioxidants (SOD and GSH) were significantly decreased in H_2O_2-injured H9c2 cells compared with those in the vehicle group. In contrast, EA-AuNP treatment attenuated these decreases and elevated the levels of SOD and GSH (Fig. 5F). In line with these results, EA-AuNP treatment also restored the MDA content to normal levels. These results suggested that EA-AuNP treatment can attenuate H_2O_2-induced oxidative stress injuries by increasing the activity of free radical scavenging enzymes in cardiomyocytes.

The expression of apoptosis-related proteins, including anti-apoptotic Bcl-2, pro-apoptotic Bax, and cleaved caspase-3, was evaluated by western blot analysis to further clarify the protective effects of EA-AuNP treatment. At the molecular biology level, EA-AuNP treatment reversed the downregulation of Bcl-2 induced by H_2O_2 and suppressed the upregulation of Bax, leading to a decreased Bax/Bcl-2 ratio (Fig. 5G). EA-AuNP treatment also markedly resulted in a 2.15-fold decrease in the expression of cleaved caspase-3 compared with the H_2O_2 group. These results further demonstrated the anti-apoptotic effect of EA-AuNP treatment on H9c2 cells subjected to oxidative stress.

The endogenous lipids of various groups were also identified using HPLC-Q-TOF-MS, and the lipid contents of each sample are detailed in Table S1. The specific content of each lipid category is shown in Fig. 6A. Compared to the H_2O_2 group, the EA-AuNP group presented significant decreases in the contents of Cer[NS], sphingomyelin (SM), phosphatidylcholine (PC), ether-phosphatidylcholine (EtherPC), and monoglyceride (MG), closely with the levels detected in the control group. Partial least squares-discriminant analysis (PLS-DA) presented a clear separation between the control group and the H_2O_2

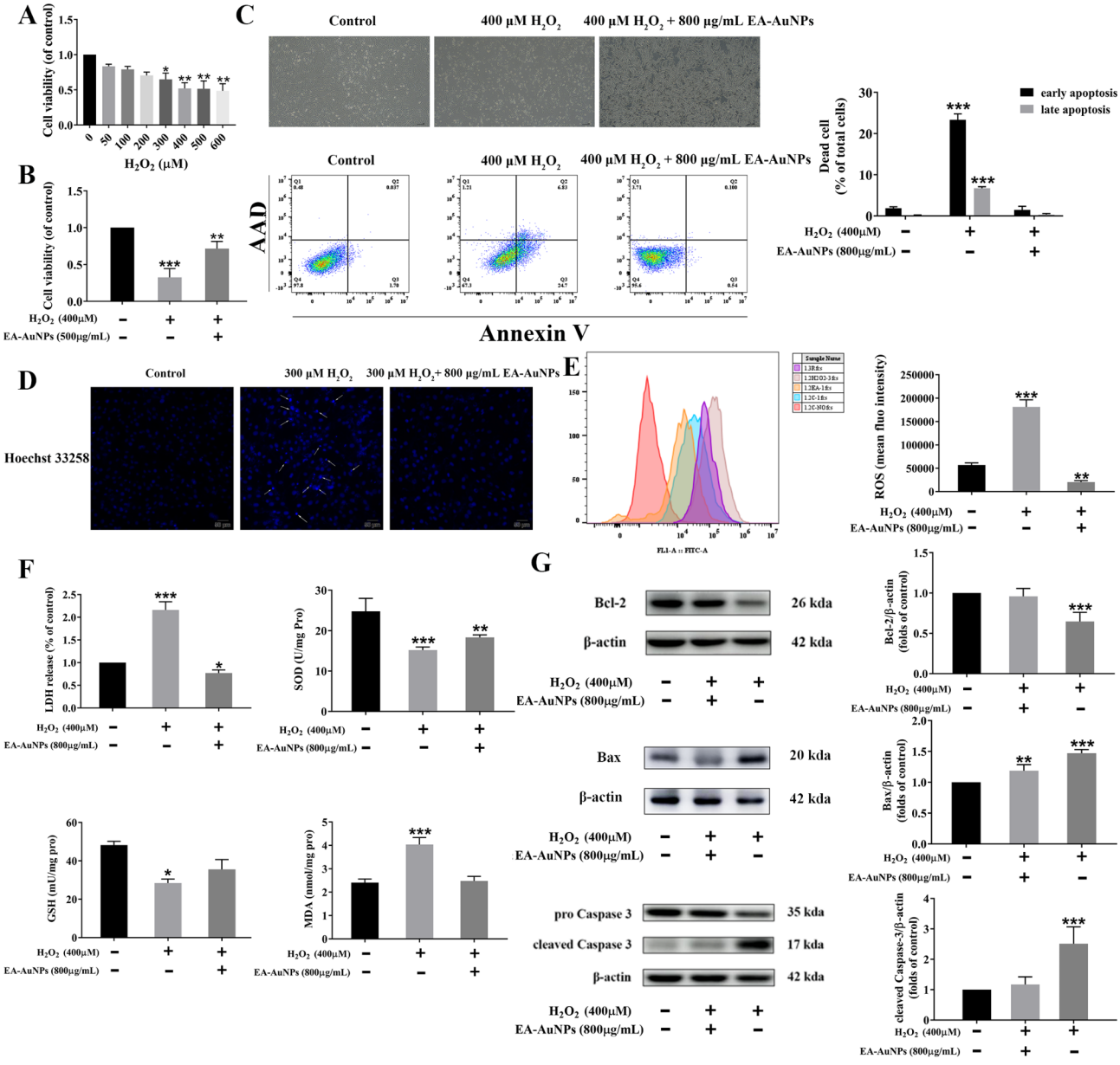

Fig. 5 Anti-apoptosis and ROS scavenging abilities of EA-AuNPs in cardiomyocytes. (**A**) Viability of H9c2 cells incubated with different concentrations of H_2O_2 for 24 h. (**B**) EA-AuNPs protect H9c2 cells from H_2O_2-induced cytotoxicity. (**C**) Representative photographs and flow cytometry results showing H9c2 cells apoptosis under EA-AuNPs treatment by using an Annexin V-FITC/AAD staining assay. (**D**) Representative fluorescence micrographs of Hoechst 33,258-stained H9c2 cells treated with 400 μM H_2O_2 for 12 h with or without EA-AuNP treatment. (**E**) Intracellular ROS levels in H9c2 cells treated with 400 μM H_2O_2 for 12 h with or without EA-AuNP treatment. 1.3R: Rousup group; 1.2H_2O_2: H_2O_2 group; 1.2EA: EA-AuNPs group; 1.2 C-1: control group; 1.2 C-NO: non-probe group. (**F**) Effect of EA-AuNPs on the SOD, LDH, MDA, and GSH levels in H9c2 cells treated with H_2O_2 for 12 h. (**G**) Effect of EA-AuNPs on the protein expression of Bcl-2, Bax, and caspase-3 in H_2O_2-treated H9c2 cells. Values are mean ± SEM ($n = 6$); *$p < 0.05$, **$p < 0.01$, ***$p < 0.001$ vs. control group

group (Fig. 6B), but the EA-AuNP group was located close to the control group, revealing significant modulation of lipid contents in H9c2 cells following EA-AuNP treatment. The heatmap with unsupervised hierarchical clustering (Fig. 6C) depicted consistent results; the EA-AuNP and control groups showed similar lipid profiles, forming two main clusters (the H_2O_2 group on the left, and the EA-AuNP and control groups on the right). A cut-off VIP value of 1.4 was selected to identify the most responsive lipids for classification among these groups: 37 lipid molecules were altered in these three groups (Fig. 6D), with the highest value being PC (16:1/22:6), followed by Cer (18:2;2O/24:1). To further screen the potential efficacy-related lipid biomarkers in MI mice after EA-AuNP treatment, the VIP value, P value, and FC value (VIP > 1, $p < 0.05$, FC > 1.5 or < -1.5) were selected

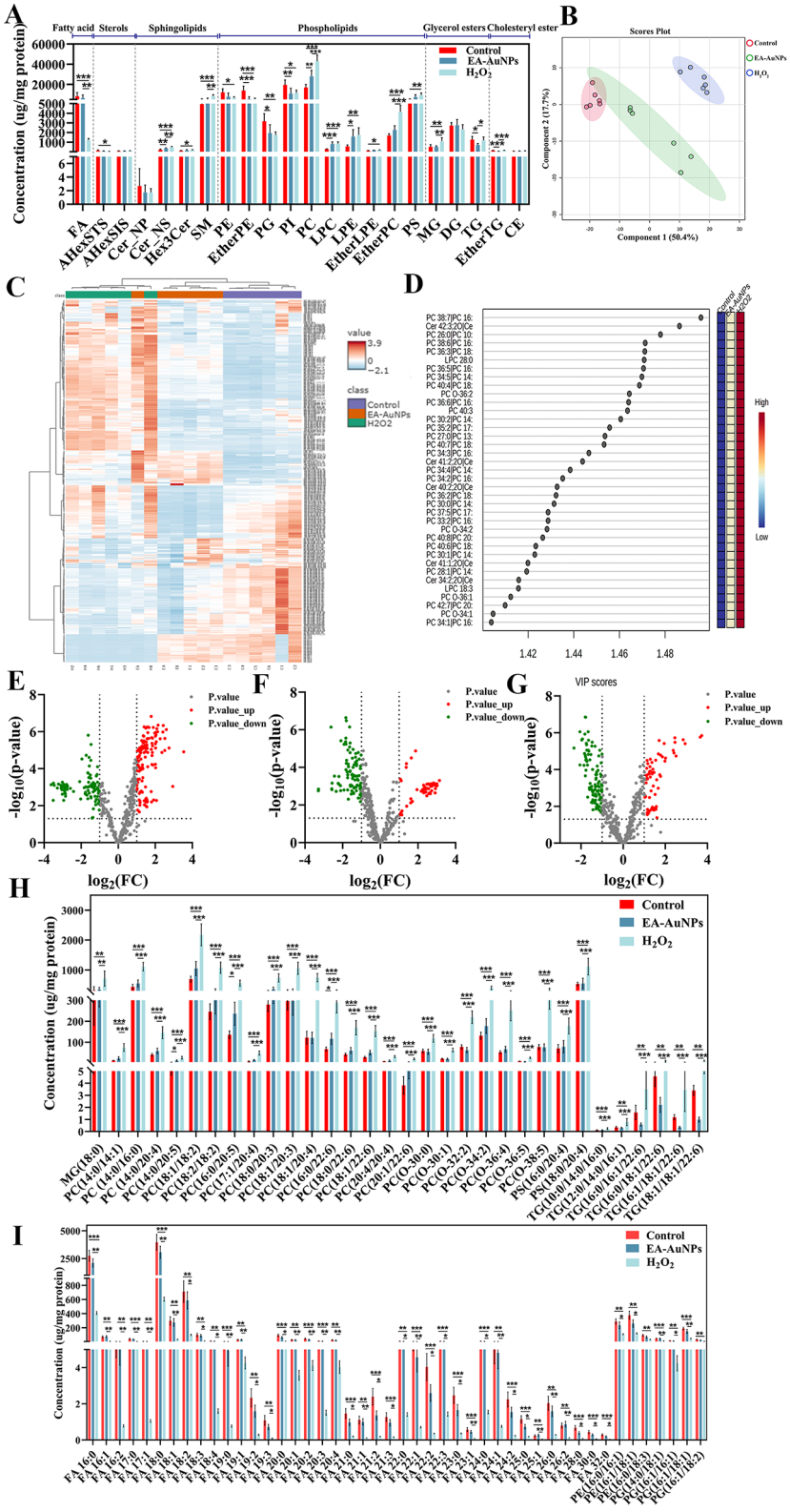

Fig. 6 Effect of EA-AuNPs on the lipid profiles of cardiomyocytes in the ROS microenvironment. (**A**) The impact of EA-AuNP treatment on the content of each lipid category in H_2O_2-induced H9c2 cells. (**B**) PLS-DA score plot. (**C**) Heatmap with unsupervised hierarchical clustering. (**D**) Important feature plot identified by PLS-DA. (**E**) Volcano plot of lipids between the H_2O_2 group and the control group. (**F**) Volcano plot of lipids between the EA-AuNP group and the H_2O_2 group. (**F**) Volcano plot of lipids between the EA-AuNP group and the control group. (**G**) The concentration of 32 reversed lipids (up-regulated in the H_2O_2 group compared with the control group) after EA-AuNP treatment. (**H**) The concentration of 46 reversed lipids (down-regulated in the H_2O_2 group compared with the control group) after EA-AuNP treatment. Values are mean ± SEM ($n = 6$); $^*p < 0.05$, $^{**}p < 0.01$, $^{***}p < 0.001$ vs. control group

to narrow the filtering threshold. Volcano plots (Fig. 6E) revealed 238 differential lipid molecules, including 110 down-regulated and 128 up-regulated in the H_2O_2 group compared to the control group, while EA-AuNP treatment clearly minimized the number of the up-regulated lipids (Fig. 6F, G). Further volcano plot analysis presented that 78 potential lipid markers (32 up-regulated and 46 down-regulated in the H_2O_2 group) were reversed after EA-AuNP treatment (detailed in Fig. 6H and I), while the majority of the residual lipids also tended to converge toward the levels in the control group. As a result, the disrupted homeostasis of lipid profiles in the H_2O_2 group can be restored by EA-AuNP treatment via adjustments involving potential efficacy-related lipid biomarkers.

Oxylipin profiling of serum samples from MI mice

Oxylipins, a class of metabolites derived from polyunsaturated fatty acid oxygenation [58], are crucial for various physiological processes, including vascular, immunological, and inflammatory responses, and are involved in many important cardiovascular disease (CVD) pathologies [59, 60]. Twenty oxylipins were quantified in all groups using HPLC-QQQ-MS analysis, including 8 arachidonic acid (AA) metabolites, 3 eicosapentaenoic acid (EPA) metabolites, 3 docosahexaenoic acid (DHA) metabolites, and 6 linoleic acid (LA) metabolites. Representative MRM chromatograms of the oxylipins detected in the selected mouse serum samples are shown in Fig. 7A. To explore the differential expression of oxylipins between the control and ISO groups, pairwise comparisons were used to analyze oxylipin concentrations. Volcano plots identified five significantly downregulated oxylipins (FC < -1.5 and $p<0.05$), namely, 14,15-EET, 5-HEPE, 4-HDHA, 12-HEPE, and 17-HDHA (Fig. 7B).

We further investigated the effects of EA-AuNPs on the perturbed oxylipins in ISO-induced oxidative damage mice to explore the potential bioactive impact-related mechanism of EA-AuNP treatment. Fig. 7C describes the distribution of oxylipins by parent fatty acids as a percentage of the total oxylipin amount in all groups. Compared with that in the control group, the percentage of LA-oxylipins was significantly increased in both the ISO and AuNP groups. The proportions of oxylipins in the control and L-EA-AuNP groups were similar, with nearly constant percentages among the AA, EPA, and DHA-oxylipin groups. The distributions of AA, EPA, DHA, and LA-derived oxylipins are presented in Fig. 7D and Table S2. The HEPEs dramatically decreased in the ISO and AuNP groups, whereas they markedly increased in the L-EA-AuNP group. These compounds, biosynthesized from EPA by different oxygenases, include at least three HEPEs (i.e., 5-HEPE, 12-HEPE, and 18-HEPE) with biological activities related to glucose metabolism or cardioprotection. The EPA metabolite 12-HEPE has been reported to inhibit atherosclerosis development by preventing macrophage transformation into foam cells [61]. Similarly, the L-EA-AuNP group exhibited significantly up-regulated levels of DHA-derived oxylipins, 14-HDHA and 17-HDHA ($p<0.01$). Recently, 14-HDHA and 17-HDHA were reported to exert their anti-inflammatory effects on neutrophil and monocyte/macrophage recruitment via the N-formyl peptide receptor 2 [62]. It is also documented that DHA and its 12-LOX-derived oxylipins, 11-HDHA and 14-HDHA, attenuate platelet aggregation and thrombus formation [63]. Interestingly, the concentration of the anti-inflammatory 14,15-EET [64] was also significantly elevated in the L-EA-AuNPs group compared with the ISO group. Many studies have shown the thrombolytic and vasodilatory characteristics of EETs within the vasculature [65].

We employed multivariate statistical analysis to further explore lipid alterations among various groups and evaluate whether EA-AuNP treatment can ameliorate perturbed oxylipins in ISO-administered mice. The supervised PLS-DA score plot (Fig. 7E) demonstrated a strong correlation among the control, L-EA-AuNP, and H-EA-AuNP groups (with a relatively large overlap). Moreover, clear separations were found between the L-EA-AuNP and ISO groups, indicating that EA-AuNP (100 mg/kg) treatment intervened in ISO-induced oxylipin perturbations. Additionally, there was substantial overlap between the H-EA-AuNP group and both the control and ISO groups, demonstrating that the oxylipin profile of the H-EA-AuNP group was intermediate between the two, similar to the results depicted in Fig. 7C. Consistent results were revealed in a heatmap with unsupervised hierarchical clustering; two main clusters (control, L-EA-AuNP, and H-EA-AuNP groups on the left; ISO and AuNP groups on the right) demonstrated similar oxylipin profiles between the control and EA-AuNP treatment groups (Fig. 7F). Moreover, we conducted a detailed analysis to identify differential oxylipins between the L-EA-AuNP and ISO groups, aiming to find putative targets implicated in the bioactive effects of EA-AuNP treatment. A volcano plot (Fig. 7G) identified 10 significantly up-regulated oxylipins (VIP>1, $p<0.05$, FC>1 or < -1), which included all of the EPA- and DHA-oxylipins. Interestingly, all oxylipins that showed down-regulation after ISO induction exhibited significant up-regulation in the L-EA-AuNP group, suggesting that these oxylipin-related pathways may be responsible for the bioactive effects of EA-AuNPs.

Conclusion

In summary, we have successfully synthesized multilayer core-shell gold nanoparticles with enhanced biocompatibility and bioactivity through the incorporation of ellagic acid, achieving high dispersion. We found that

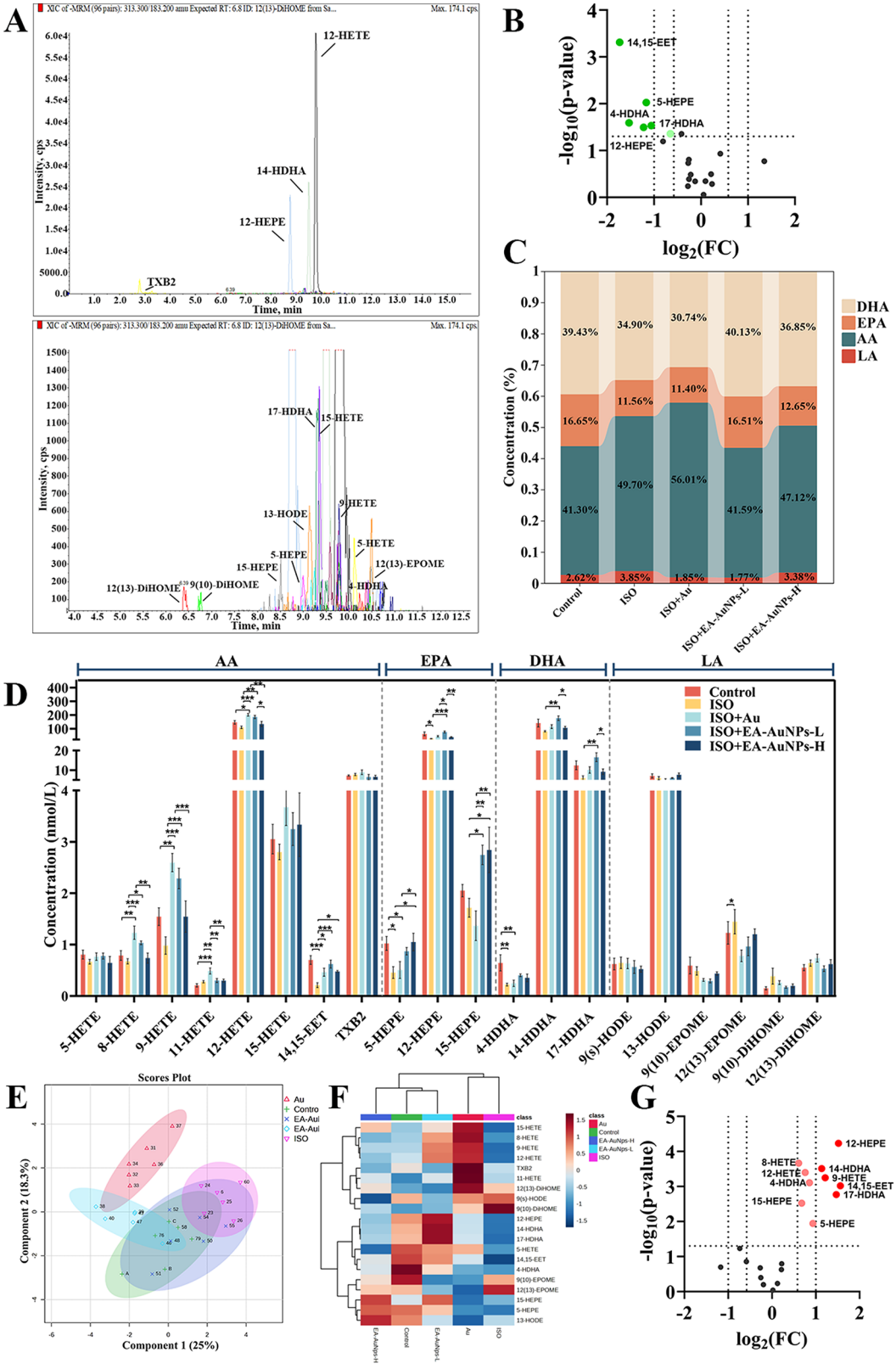

Fig. 7 EA-AuNP pretreatment restores perturbed oxylipins in MI mice. (**A**) Representative MRM chromatograms for each identified oxylipin in mouse serum. (**B**) Volcano plot of oxylipins between the ISO group and the control group. (**C**) Distribution of oxylipins by parent fatty acids as a percent of the whole total oxylipin amount. (**D**) The impact of EA-AuNP treatment on the AA-, EPA-, DHA-, and LA- oxylipins in ISO-administered mice. (**E**) PLS-DA score plot. (**F**) Heatmap with unsupervised hierarchical clustering. (**G**) Volcano plot of oxylipins between the L-EA-AuNP group and the ISO group. Values are mean ± SEM ($n = 6$); *$p < 0.05$, **$p < 0.01$, ***$p < 0.001$ vs. control group

EA-AuNPs exhibit superior cytocompatibility to THP-1 and H9c2 cells and enable a desirable excretion-based metabolism without overburdening other organs. EA-AuNPs also demonstrated anti-apoptotic effects, protecting cardiomyocytes against H_2O_2-induced oxidative stress. In vitro results proved that EA-AuNP treatment increased the activity of free radical scavenging enzymes in cardiomyocytes and exhibited excellent ROS scavenging properties. Correspondingly, EA-AuNP treatment effectively ameliorated oxidative stress injuries in MI mice by inhibiting the ISO-induced elevation of cardiac enzyme activities and enhancing the antioxidant capacity of cardiomyocytes. Furthermore, our studies showed that EA-AuNPs can restore the perturbed anti-inflammatory oxylipins in MI mice, suggesting that the bioactive effects of EA-AuNPs on MI mice may be mediated through the regulation of these oxylipins. Taken together, our current studies not only highlighted the superior bioactive effects of EA-AuNPs in myocardial injury but also contributed to the development of novel gold-phenolic core-shell nanoparticles, further advancing their potential medical applications.

Supplementary Information

The online version contains supplementary material available at https://doi.org/10.1186/s12951-024-02796-8.

Supplementary Material 1

Supplementary Material 2

Acknowledgements

This research was financially supported by the Macau Science and Technology Development Fund (0050/2020/AFJ) and the Science and Technology Development Fund, Macau SAR (006/2023/SKL). The funders had no role in study design, data collection, and analysis, decision to publish, or preparation of the manuscript. The authors also thank the Department of Science and Technology of Guangdong Province for the support of Guangdong-HongKong-Macao Universities Joint Laboratory for Internationalization of TCM (2023LSYS002).

Author contributions

Y.X.N. proposed, planned, and executed experiments, prepared materials, analyzed data, and wrote the the original draft. W.J. assisted with the lipidomic analysis and oxylipin profiling. W.T.T. assisted with the animal experiments. S.S.S. assisted with cell culture experiments. S.H.N. assisted with assembly efficiency determination of nanoparticles. H.H. supervised the research. L.P. supervised the research, participated in discussions, revised the manuscript, and provided funding.

Funding

This research was financially supported by the Macau Science and Technology Development Fund (0050/2020/AFJ) and the Science and Technology Development Fund, Macau SAR (006/2023/SKL). The funders had no role in study design, data collection, and analysis, decision to publish, or preparation of the manuscript.

Data availability

No datasets were generated or analysed during the current study.

Declarations

Ethics approval and consent to participate

All animal experiments were approved by the local Animal Ethics Committees of the State Key Laboratories for Quality Research in Chinese Medicines, Macau University of Science and Technology (Approved number: 072/DICV/DIS/2021).

Consent for publication

Not applicable.

Competing interests

The authors declare no competing interests.

Author details

[1]State Key Laboratory of Quality Research in Chinese Medicine, School of Pharmacy, Macau University of Science and Technology, Macau, China
[2]Key Laboratory of Oilseeds Processing of Ministry of Agriculture, Hubei Key Laboratory of Lipid Chemistry and Nutrition, Oil Crops Research Institute of the Chinese Academy of Agricultural Sciences, Wuhan, Hubei, China
[3]Guangdong-Hong Kong-Macao Universities Joint Laboratory for the Internationalization of Traditional Chinese Medicine, Jinan University, Guangzhou, China
[4]Department of Cardiology, The Eighth Affiliated Hospital, Joint Laboratory of Guangdong-HongKong-Macao, Universities for Nutritional Metabolism and Precise Prevention and Control of Major Chronic Diseases, Sun Yat-sen University, Shenzhen, China

Received: 3 June 2024 / Accepted: 20 August 2024
Published online: 11 September 2024

References

1. Puymirat E, Simon T, Cayla G, Cottin Y, Elbaz M, Coste P, et al. Acute myocardial infarction: changes in patient characteristics, management, and 6-month outcomes over a period of 20 years in the FAST-MI program (French Registry of Acute ST-Elevation or Non-ST-Elevation myocardial infarction) 1995 to 2015. Circulation. 2017;136:1908–19.
2. Senyo SE, Steinhauser ML, Pizzimenti CL, Yang VK, Cai L, Wang M, et al. Mammalian heart renewal by pre-existing cardiomyocytes. Nature. 2013;493:433–6.
3. Rurik JG, Tombácz I, Yadegari A, Méndez Fernández PO, Shewale SV, Li L, et al. CAR T cells produced in vivo to treat cardiac injury. Science. 2022;375:91–6.
4. Chouchani ET, Pell VR, Gaude E, Aksentijević D, Sundier SY, Robb EL, et al. Ischaemic accumulation of succinate controls reperfusion injury through mitochondrial ROS. Nature. 2014;515:431–5.
5. Hausenloy DJ, Yellon DM. Myocardial ischemia-reperfusion injury: a neglected therapeutic target. J Clin Investig. 2013;123:92–100.
6. Zhang Z, Zhao X, Gao M, Xu L, Qi Y, Wang J, et al. Dioscin alleviates myocardial infarction injury via regulating BMP4/NOX1-mediated oxidative stress and inflammation. Phytomedicine. 2022;103:154222.
7. Frantz S, Hundertmark MJ, Schulz-Menger J, Bengel FM, Bauersachs J. Left ventricular remodelling post-myocardial infarction: pathophysiology, imaging, and novel therapies. Eur Heart J. 2022;43:2549–61.
8. Martin TP, MacDonald EA, Elbassioni AAM, O'toole D, Zaeri AAI, Nicklin SA, et al. Preclinical models of myocardial infarction: from mechanism to translation. Brit J Pharmacol. 2022;179:770–91.
9. Barbato E, Mehilli J, Sibbing D, Siontis GC, Collet JP, Thiele H, et al. Questions and answers on antithrombotic therapy and revascularization strategies in non-ST-elevation acute coronary syndrome (NSTE-ACS): a companion document of the 2020 ESC guidelines for the management of acute coronary syndromes in patients presenting without persistent ST-segment elevation. Eur Heart J. 2021;42:1368–78.
10. Heusch G. Myocardial ischaemia-reperfusion injury and cardioprotection in perspective. Nat Rev Cardiol. 2020;17:773–89.
11. Nian M, Lee P, Khaper N, Liu P. Inflammatory cytokines and postmyocardial infarction remodeling. Circ Res. 2004;94:1543–53.
12. Sager HB, Hulsmans M, Lavine KJ, Moreira MB, Heidt T, Courties G, et al. Proliferation and recruitment contribute to myocardial macrophage expansion in chronic heart failure. Circ Res. 2016;119:853–64.

13. Tang N, Ding Z, Zhang S, Luo D, Liu X, Bao X, et al. Nanoassemblies Derived from Natural Flavonoid compounds as new antioxidant oral preparations for targeted inflammatory bowel Disease Therapy. Adv Funct Mater. 2023;33:2305133.
14. Ben-Mordechai T, Kain D, Holbova R, Landa N, Levin LP, Elron-Gross I, et al. Targeting and modulating infarct macrophages with hemin formulated in designed lipid-based particles improves cardiac remodeling and function. J Controlled Release. 2017;257:21–31.
15. Ding L, Yao C, Yin X, Li C, Huang Y, Wu M, et al. Size, shape, and protein corona determine cellular uptake and removal mechanisms of gold nanoparticles. Small. 2018;14:1801451.
16. Chen J, Ma Y, Du W, Dai T, Wang Y, Jiang W, et al. Furin-instructed intracellular gold nanoparticle aggregation for tumor photothermal therapy. Adv Funct Mater. 2020;30:2001566.
17. Nie Z, Petukhova A, Kumacheva E. Properties and emerging applications of self-assembled structures made from inorganic nanoparticles. Nat Nanotechnol. 2010;5:15–25.
18. Love JC, Estroff LA, Kriebel JK, Nuzzo RG, Whitesides GM. Self-assembled monolayers of thiolates on metals as a form of nanotechnology. Chem Rev. 2005;105:1103–70.
19. Duan H, Wang D, Li Y. Green chemistry for nanoparticle synthesis. Chem Soc Rev. 2015;44:5778–92.
20. Chung CH, Jung W, Keum H, Kim TW, Jon S. Nanoparticles derived from the natural antioxidant rosmarinic acid ameliorate acute inflammatory bowel disease. ACS Nano. 2020;14:6887–96.
21. Dai Q, Geng H, Yu Q, Hao J, Cui J. Polyphenol-based particles for theranostics. Theranostics. 2019;9:3170.
22. Zhou J, Lin Z, Ju Y, Rahim MA, Richardson JJ, Caruso F. Polyphenol-mediated assembly for particle engineering. Acc Chem Res. 2020;53:1269–78.
23. Zhao Z, Pan DC, Qi QM, Kim J, Kapate N, Sun T, et al. Engineering of living cells with polyphenol-functionalized biologically active nanocomplexes. Adv Mater. 2020;32:2003492.
24. Ren C, Gao Y, Guan Y, Wang Z, Yang L, Gao J, et al. Carrier-free supramolecular hydrogel composed of dual drugs for conquering drug resistance. ACS Appl Mater Interfaces. 2019;11:33706–15.
25. Qi Y, Li J, Nie Q, Gao M, Yang Q, Li Z, et al. Polyphenol-assisted facile assembly of bioactive nanoparticles for targeted therapy of heart diseases. Biomaterials. 2021;27:120952.
26. Luo CL, Liu YQ, Wang P, Song C, Wang KJ, Dai LP, et al. The effect of quercetin nanoparticle on cervical cancer progression by inducing apoptosis, autophagy and anti-proliferation via JAK2 suppression. Biomed Pharmacother. 2016;82:595–605.
27. Liu Y, Zhang X, Wu T, Liu B, Yang J, Liu W. Chinese herb-crosslinked hydrogel bearing rBMSCs-laden polyzwitterion microgels: self-adaptive manipulation of micromilieu and stemness maintenance for restoring infarcted myocardium. Nano Today. 2021;41:101306.
28. Bligh EG, Dyer WJ. A rapid method of total lipid extraction and purification. Can J Biochem Physiol. 1959;37:911–7.
29. Wu ZY, Xiao HM, Rao D, Wang J, Lv X, Wang D, et al. Analytical strategy for oxylipin annotation by combining chemical derivatization-based retention index algorithm and feature tandem mass spectrometric fragmentation as a biomarker discovery tool. Anal Chem. 2023;95:15933–42.
30. Daniel MC, Astruc D. Gold nanoparticles: assembly, supramolecular chemistry, quantum-size-related properties, and applications toward biology, catalysis, and nanotechnology. Chem Rev. 2004;104:293–346.
31. Saha K, Agasti SS, Kim C, Li X, Rotello VM. Gold nanoparticles in chemical and biological sensing. Chem Rev. 2012;112:2739–79.
32. Wang Y, Sun SK, Liu Y, Zhang Z. Advanced hitchhiking nanomaterials for biomedical applications. Theranostics. 2023;13:4781.
33. Wang Y, Quinsaat JEQ, Ono T, Maeki M, Tokeshi M, Isono T, et al. Enhanced dispersion stability of gold nanoparticles by the physisorption of cyclic poly (ethylene glycol). Nat Commun. 2020;11:6089.
34. Zhang X, Servos MR, Liu J. Ultrahigh nanoparticle stability against salt, pH, and solvent with retained surface accessibility via depletion stabilization. J Am Chem Soc. 2012;134:9910–3.
35. Sadalage PS, Patil RV, Havaldar DV, Gavade SS, Santos AC, Pawar KD. Optimally biosynthesized, PEGylated gold nanoparticles functionalized with quercetin and camptothecin enhance potential anti-inflammatory, anti-cancer and anti-angiogenic activities. J Nanobiotechnol. 2021;19:1–17.
36. Barai AC, Paul K, Dey A, Manna S, Roy S, Bag BG, et al. Green synthesis of Nerium oleander-conjugated gold nanoparticles and study of its in vitro anticancer activity on MCF-7 cell lines and catalytic activity. Nano Convergence. 2018;5:1–9.
37. Aratboni HA, Rafiei N, Khorashad LK, Lerma-Escalera I, Balderas-Cisneros FDJ, Liu Z, et al. LED control of gene expression in a nanobiosystem composed of metallic nanoparticles and a genetically modified E. Coli strain. J Nanobiotechnol. 2021;19:190.
38. Chokkareddy R, Redhi GG. Green synthesis of metal nanoparticles and its reaction mechanisms, Green metal nanoparticles: synthesis, characterization and their applications. 2018. p. 113–39.
39. Imran M, Shah MR, Ullah F, Ullah S, Elhissi AM, Nawaz W, et al. Sugar-based novel niosomal nanocarrier system for enhanced oral bioavailability of levofloxacin. Drug Delivery. 2016;23:3653–64.
40. Tao JS, Wei ZJ, He Y, Yan XY, Lee SMY, Wang XQ, et al. Toward understanding the prolonged circulation and elimination mechanism of crosslinked polymeric micelles in zebrafish model. Biomaterials. 2020;256:120180.
41. Poon W, Zhang YN, Ouyang B, Kingston BR, Wu JLY, Wilhelm S, et al. Elimination pathways of nanoparticles. ACS Nano. 2019;13:5785–98.
42. He T, Niu N, Chen Z, Li S, Liu S, Li J. Novel quercetin aggregation-induced emission luminogen (AIEgen) with excited-state intramolecular proton transfer for in vivo bioimaging. Adv Funct Mater. 2018;28:1706196.
43. Lu G, Wang X, Cheng M, Wang S, Ma K. The multifaceted mechanisms of ellagic acid in the treatment of tumors: state-of-the-art. Biomed Pharmacother. 2023;165:115132.
44. Mannino F, Imbesi C, Bitto A, Minutoli L, Squadrito F, D'Angelo T. Anti-oxidant and anti-inflammatory effects of ellagic and punicic acid in an in vitro model of cardiac fibrosis. Biomed Pharmacother. 2023;162:114666.
45. Gupta A, Singh AK, Kumar R, Jamieson S, Pandey AK, Bishayee A. Neuroprotective potential of ellagic acid: a critical review. Adv Nutr. 2021;12:1211–38.
46. Wei D, Lin C, Huang Y, Wu L, Huang M. Ellagic acid promotes ventricular remodeling after acute myocardial infarction by up-regulating miR-140-3p. Biomed Pharmacother. 2017;95:983–9.
47. Bala I, Bhardwaj V, Hariharan S, Kumar MNVR. Analytical methods for assay of ellagic acid and its solubility studies. J Pharmaceut Biomed. 2006;40:206–10.
48. Furtado D, Björnmalm M, Ayton S, Bush AI, Kempe K, Caruso F. Overcoming the blood–brain barrier: the role of nanomaterials in treating neurological diseases. Adv Mater. 2018;30:1801362.
49. Dong K, Zhang Y, Zhang L, Wang Z, Ren J, Qu X. Facile preparation of metal–organic frameworks-based hydrophobic anticancer drug delivery nanoplatform for targeted and enhanced cancer treatment. Talanta. 2019;194:703–8.
50. Rona G. An infarct-like myocardial lesion and other toxic manifestations produced by isoproterenol in the rat. AMA Arch Pathol. 1959;67:443–55.
51. Hill JA, Karimi M, Kutschke W, Davisson RL, Zimmerman K, Wang Z, et al. Cardiac hypertrophy is not a required compensatory response to short-term pressure overload. Circulation. 2000;101:2863–9.
52. Hao T, Qian M, Zhang YT, Liu Q, Midgley AC, Liu YP, et al. An Injectable Dual-Function Hydrogel Protects against Myocardial Ischemia/Reperfusion Injury by modulating ROS/NO disequilibrium. Adv Sci. 2022;9:2105408.
53. Hu C, Liu WQ, Long LY, Wang ZC, Zhang W, He SY, et al. Regeneration of infarcted hearts by myocardial infarction-responsive injectable hydrogels with combined anti-apoptosis, anti-inflammatory and pro-angiogenesis properties. Biomaterials. 2022;290:121849.
54. Park SJ, Kim RY, Park BW, Lee S, Choi SW, Park JH, et al. Dual stem cell therapy synergistically improves cardiac function and vascular regeneration following myocardial infarction. Nat Commun. 2019;10:3123.
55. Guo Y, Sun Q, Wu FG, Dai Y, Chen X. Polyphenol-containing nanoparticles: synthesis, properties, and therapeutic delivery. Adv Mater. 2021;33:2007356.
56. Geng ZH, Huang L, Song MB, Song YM. Cardiovascular effects in vitro of a polysaccharide from Salvia miltiorrhiza. Carbohydr Polym. 2015;121:241–7.
57. Qin F, Liu YX, Zhao HW, Huang X, Ren P, Zhu ZY. Chinese medicinal formula Guan-Xin-Er-Hao protects the heart against oxidative stress induced by acute ischemic myocardial injury in rats. Phytomedicine. 2009;16:215–21.
58. Buczynski MW, Dumlao DS, Dennis EA. An integrated omics analysis of eicosanoid biology. J Lipid Res. 2009;50:1015–38.
59. Serhan CN. Pro-resolving lipid mediators are leads for resolution physiology. Nature. 2014;510:92–101.
60. Ma K, Yang J, Shao Y, Li P, Guo H, Wu J, et al. Therapeutic and prognostic significance of arachidonic acid in heart failure. Circ Res. 2022;130:1056–71.
61. Nagatake T, Shibata Y, Morimoto S, Node E, Sawane K, Hirata SI, et al. 12-Hydroxyeicosapentaenoic acid inhibits foam cell formation and ameliorates high-fat diet-induced pathology of atherosclerosis in mice. Sci Rep. 2021;11:10426.

62. Shu T, Zhang J, Zhou Y, Chen Z, Li J, Tang Q, et al. Eosinophils protect against pulmonary hypertension through 14-HDHA and 17-HDHA. Eur Respir J. 2023;61:2200582.
63. Yamaguchi A, Stanger L, Freedman CJ, Standley M, Hoang T, Adili R, et al. DHA 12-LOX-derived oxylipins regulate platelet activation and thrombus formation through a PKA-dependent signaling pathway. J Thromb Haemost. 2021;19:839–51.
64. Lai J, Chen C. The role of epoxyeicosatrienoic acids in cardiac remodeling. Front Physiol. 2021;12:642470.
65. Imig JD. Epoxides and soluble epoxide hydrolase in cardiovascular physiology. Physiol Rev. 2012;92:101–30.

Publisher's note